

Article

Convergence of (Soft) Elastohydrodynamic Lubrication Simulations of Textured Slider Bearings

Quentin Allen ^{1,*} and Bart Raeymaekers ²¹ Department of Manufacturing Engineering, Brigham Young University, Provo, UT 84602, USA² Department of Mechanical Engineering, Virginia Tech, Blacksburg, VA 24061, USA

* Correspondence: quentin_allen@byu.edu

Abstract: We study the convergence of elastohydrodynamic lubrication (EHL) simulations of textured slider bearings. EHL simulations are computationally expensive because the equations that describe the lubricant film pressure and the deformation of the bearing surfaces are coupled and, thus, must be solved simultaneously. Additional simulation requirements, such as maintaining a specific bearing load-carrying capacity or lubricant film thickness, further increase the computational cost because they impose additional constraints or add equations that must converge simultaneously with those that describe the lubricant film pressure and bearing surface deformation. We methodically quantify the convergence of EHL simulations of textured slider bearings as a function of simulation parameters, including different convergence metrics and criteria, but also cavitation models, texture design parameters, and bearing operating parameters. We conclude that the interplay between discretization, the convergence metric, and the convergence criterion must be carefully considered to implement numerical simulations that converge to the correct physical solution. Our analysis also illustrates that a well-designed convergence study can minimize the computational cost.

Keywords: elastohydrodynamic lubrication; EHL; numerical simulation; convergence



Citation: Allen, Q.; Raeymaekers, B. Convergence of (Soft) Elastohydrodynamic Lubrication Simulations of Textured Slider Bearings. *Lubricants* **2023**, *11*, 92. <https://doi.org/10.3390/lubricants11030092>

Received: 29 December 2022

Revised: 6 February 2023

Accepted: 17 February 2023

Published: 21 February 2023



Copyright: © 2023 by the authors. Licensee MDPI, Basel, Switzerland. This article is an open access article distributed under the terms and conditions of the Creative Commons Attribution (CC BY) license (<https://creativecommons.org/licenses/by/4.0/>).

1. Introduction

A thin lubricant film reduces the contact and friction between sliding surfaces compared to dry sliding conditions. Thus, it increases efficiency by reducing energy loss from friction and it increases longevity by reducing wear from contact. Consequently, designing lubricant films to reduce friction and wear of the bearing surfaces is of practical importance to a broad spectrum of engineering applications, including sliding interfaces in automotive components such as piston/liner pairs [1], energy generation equipment such as (wind) turbines [2], and medical devices such as prosthetic hip and knee implants [3,4], to only name a few. The literature documents many different ways to reduce friction and wear between bearing surfaces, depending on the operating and design parameters of the bearing and the lubrication regime in which it operates. Lubrication regimes can be categorized according to the physical interaction between the bearing surfaces, including boundary lubrication (BL), where the bearing load is entirely borne by solid-on-solid contact between the bearing surfaces, mixed lubrication (ML), in which the bearing load is shared between solid-on-solid contact and lubricant film pressure, and hydrodynamic lubrication (HL), where the entire bearing load is carried by the lubricant film pressure [5,6]. Elastohydrodynamic lubrication (EHL) is similar to HL but it accounts for deformable rather than rigid bearing surfaces [5,7]. Additionally, it is well-known that the addition of deterministic texture features to parallel bearing surfaces can promote the formation of (elasto) hydrodynamic lubrication because the texture features serve as lubricant reservoirs, they contain wear debris, and they create micro-hydrodynamic bearings [8].

Many experimental (see, e.g., [9]) and numerical (see, e.g., [10]) studies exist that contribute to the physical understanding of the different lubrication regimes. Numerical

simulations of lubricant films between sliding surfaces offer a time-saving alternative to performing costly experiments and allow the quantification of physical parameters that are often difficult to measure experimentally, such as lubricant film pressure and deformation of the bearing surfaces, which are crucial to the design of complex lubrication systems. This paper focuses on EHL simulations of textured bearing surfaces, which we have also analyzed in previous work, in the context of prosthetic hip implants [11–13].

Several research groups have studied or used EHL simulations of textured slider bearings. We categorize this prior work as (i) parameter studies that quantify the effect of texture design parameters on the bearing operating parameters, such as lubricant film thickness, lubricant film pressure, and load-carrying capacity (see, e.g., [14–16]); (ii) research that quantifies the effect of different cavitation models on the accuracy of the EHL lubrication models, notably comparing non-mass-conserving cavitation models such as the half-Sommerfeld (HS) and Reynolds (RE) cavitation models to mass-conserving algorithms such as the Jakobsson–Floberg–Olsson (JFO) model (see, e.g., [13,17,18]); (iii) studies that relate bearing surface deformation and lubricant film pressure and thickness to the operating parameters and lubricant properties (see, e.g., [19]); and (iv) comparisons between EHL and HL simulations (see, e.g., [20]).

EHL simulations are computationally expensive because the equations that describe the lubricant film pressure and the deformation of the bearing surfaces are coupled and, thus, must be solved simultaneously. Additional simulation requirements, such as maintaining a specific bearing load-carrying capacity or lubricant film thickness, further increase the computational cost because they impose additional constraints or add equations that must converge simultaneously with those that describe the lubricant film pressure and bearing surface deformation.

“Soft” EHL simulations include at least one highly deformable bearing surface [21], typically with an elastic modulus <1 GPa, such as a polyethylene liner in the hard-on-soft bearing of a prosthetic hip implant [11], a rubber gasket against a metal counterface [16], or even human eyelids [22]. Soft EHL simulations are even more computationally expensive than EHL simulations because the magnitude of the bearing surface deformation increases with decreasing stiffness, which increases its sensitivity to changes in the lubricant film pressure and, consequently, increases the number of iterations between the lubricant film pressure and bearing surface deformation solutions to achieve simultaneous convergence.

Numerical simulations of complex lubrication models must be verified and validated to ensure accuracy prior to their use in solving lubrication problems. Convergence studies of the discretization of the numerical solution domain must show that the simulations are stable, converge to the correct physical solution, and consistent [23]. However, while crucial to accurately solving (soft) EHL problems, no existing publications methodically analyze the convergence of (soft) EHL simulations as a function of different simulation parameters, including convergence metrics, cavitation models, texture design parameters, and bearing operating parameters. This is particularly pertinent for textured bearings, which may create steep pressure gradients in the lubricant film.

Thus, the objective of this work is to methodically evaluate the convergence of (soft) EHL simulations of textured slider bearings, as a function of convergence metrics and criterion, cavitation algorithms, texture design, and bearing operating parameters. This knowledge is crucial when implementing (soft) EHL computer code to solve complex lubrication problems with multiple surface texture designs or operating conditions, as well as when evaluating and interpreting the results of (soft) EHL simulations of textured bearing surfaces.

2. Methods and Materials

2.1. Model Description

Figure 1 schematically shows (a) an isometric view and (b) a top view of a cross-section of the EHL model that we use for convergence studies in this work, which comprises a rigid textured surface and a smooth, deformable counterface in relative motion, separated by a

thin, incompressible lubricant film. The rigid bearing surface displays a single, perfectly smooth [24], spherical texture feature. We do not consider surface topography of the bearing surfaces in between or inside the texture features since it is generally small compared to the dimensions of the texture features. The spherical texture feature geometry is entirely defined by the texture aspect ratio $\varepsilon = h_p/2r_p$ and the texture density $S_p = \pi r_p^2/4r_1^2$, with h_p as the maximum depth and r_p as the radius of the texture feature on the bearing surface [25]. r_1 is the half-length of an imaginary square unit cell around the texture feature. We also indicate the nominal bearing surface separation c , the local deformation $d(x,y)$, and the local lubricant film thickness $h(x,y)$.

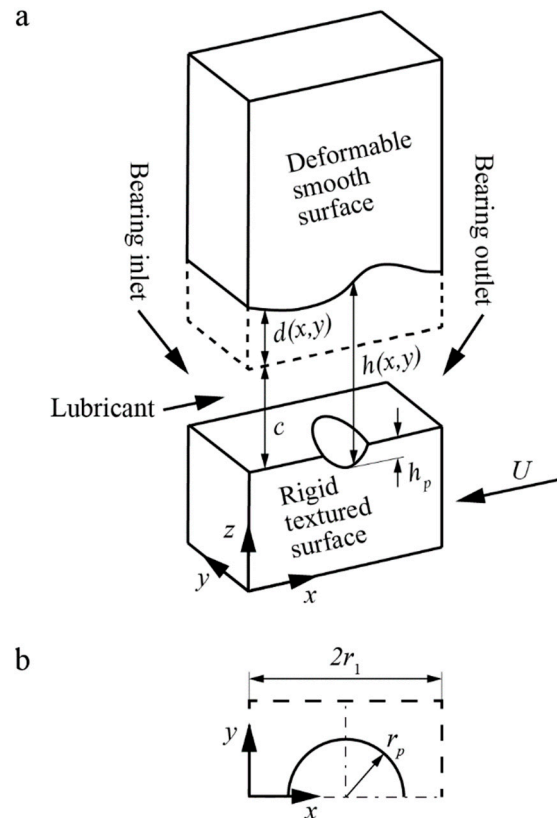


Figure 1. (a) Isometric view of the numerical simulation domain, showing a rigid textured surface and a deformable smooth surface in relative motion, separated by a fluid lubricant; (b) top view of the rigid bearing surface, indicating the texture design parameters.

We simulate the lubricant film pressure using the incompressible Reynolds equation, which represents a reduced version of the Navier–Stokes equations, specifically derived for lubrication problems [5,6]. The Reynolds equation assumes abundant supply of lubricant, the existence of a converging channel, and a separation between the bearing surfaces that is much smaller than the length-scale of the bearing. Furthermore, it assumes isothermal conditions and Newtonian lubricant viscosity. The two-dimensional, steady-state Reynolds equation is given as follows [5]:

$$\frac{\partial}{\partial x} \left(h^3 \frac{\partial p}{\partial x} \right) + \frac{\partial}{\partial y} \left(h^3 \frac{\partial p}{\partial y} \right) = 6\mu U \frac{\partial h}{\partial x} \quad (1)$$

where $p(x,y)$ is the local lubricant film pressure, μ is the dynamic viscosity of the lubricant, and U is the relative sliding velocity between the bearing surfaces.

We non-dimensionalize the Reynolds equation as

$$\frac{\partial}{\partial X} \left(H^3 \frac{\partial P}{\partial X} \right) + \frac{\partial}{\partial Y} \left(H^3 \frac{\partial P}{\partial Y} \right) = \frac{\lambda}{\delta^2} \frac{\partial H}{\partial X} \quad (2)$$

With $P = p/p_0$, $H = h/c$, $X = x/r_1$, and $Y = y/r_1$, a non-dimensional flow factor $\lambda = 3\mu U/2r_p p_0$, and non-dimensional bearing spacing $\delta = c/2r_p$. We use a central finite difference scheme on a uniform grid to solve Equation (2) over the entire solution domain. We employ a two-level grid to perform the majority of the simulations on a coarse-level grid with half as many nodes as the fine-level grid, reducing the convergence time [26]. The boundary conditions maintain atmospheric pressure ($p_0 = 101,325$ Pa, or $P = 1$) at the inlet and outlet of the bearing (x -direction) and impose symmetry on the lateral edge (y -direction) of the model to represent an infinitely wide bearing with a periodic pattern of texture features, which is similar to what we have implemented previously [11–13]. These boundary conditions are chosen to represent a common environment in engineering applications. Furthermore, because the geometry of the texture features is symmetric with respect to the centerline along the flow direction (x -direction), we only consider half of a texture feature (see Figure 1) to further reduce the computation time [25,27].

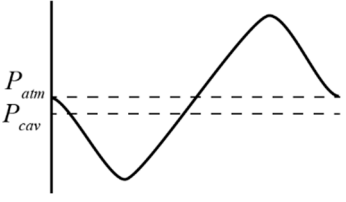
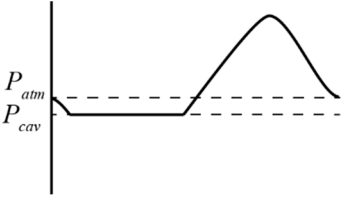
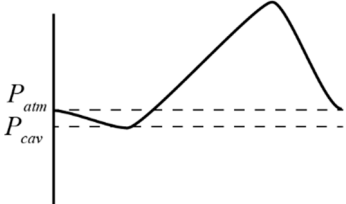
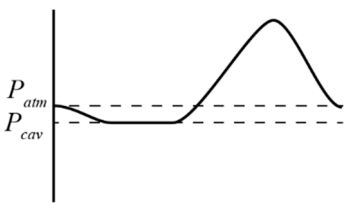
Texture features can be of any geometry, including spherical, cylindrical, or conical [12], square-, triangle-, or chevron-shaped [28], or even arbitrary-shaped based on genetic and machine learning algorithms that optimize the geometry in terms of specific objective functions, such as maximizing lubricant film thickness and stiffness, or minimizing the friction coefficient between the bearing surfaces [29,30]. However, in this work, we consider spherical texture features only, because they are easy to manufacture, using, e.g., laser surface texturing [31,32]. Furthermore, they are axisymmetric and, thus, their bearing characteristics are independent of the sliding direction, which is particularly important for bearings that do not have a preferential sliding direction, such as a prosthetic hip implant [33–35]. However, the shape of the texture features has minimal effect on the convergence of the numerical algorithm.

In addition, we define a cavitation model that describes the rupture and reformation of the lubricant film when the local lubricant film pressure decreases to the vapor pressure of water at room temperature. This is a conservative choice for the cavitation threshold that does not consider the effect of dissolved gasses in the lubricant. However, estimating a higher value of the cavitation threshold to account for gaseous cavitation may also overestimate the lubricant film pressure. We consider the HS, RE, and JFO models [5,36]. The HS model enforces the vapor pressure threshold after the numerical simulation has reached a converged solution for the local lubricant film pressure $P(X, Y)$ in Equation (2), which often results in a large cavitation region with continuous, but non-differentiable boundaries [37]. The RE model enforces the cavitation threshold in every iteration when solving Equation (2), which results in a small cavitation region with continuous and differentiable boundaries. However, both HS and RE cavitation models do not always conserve mass. In contrast, the JFO model includes additional boundary conditions to enforce mass-conservation in the cavitation region [38] and, therefore, it is considered the most physically accurate cavitation model. It is also the most prone to convergence problems [13]. A common algorithm for the JFO cavitation model was described by Elrod [39] and updated by Wang et al. [38], which adds a fractional film content parameter, $0 \leq \theta \leq 1$, to the right-hand side of Equation (2), i.e.,

$$\frac{\partial}{\partial X} \left(H^3 \frac{\partial P}{\partial X} \right) + \frac{\partial}{\partial Y} \left(H^3 \frac{\partial P}{\partial Y} \right) = \frac{\lambda}{\delta^2} \frac{\partial}{\partial X} (\theta H) \quad (3)$$

Equation (3) considers a full film regime and a cavitation regime. In the full film regime, $\theta = 1$ and Equation (3) is equivalent to the Reynolds equation of Equation (2). In the cavitation regime, the lubricant film pressure, $P = P_{cav}$ and Equation (3) considers $0 \leq \theta \leq 1$. Table 1 illustrates the different cavitation models:

Table 1. Comparison of the three cavitation models considered in this paper.

Cavitation Model	Cross-Section View of Lubricant Film Pressure	Cavitation Boundary Conditions
None		N/A
HS [37]		$P = P_{cav}$
RE [11]		$P = P_{cav}, dP/dX = 0$
JFO [38]		$P = P_{cav}, dP/dX = 0, \text{ mass conservation}$

We quantify the deformation of the soft bearing surface by solving the elastic equations (i.e., Hooke's law) with a linear elastic finite element (FE) model using 20-node brick-type elements with quadratic shape functions. We apply the lubricant film pressure calculated from Equation (2) or Equation (3) as a pressure force on the deformable bearing surface and rigidly constrain the opposite face in the FE model. We constrain rotation and deformation in the x - and y -directions and solve the elastic deformation in the z -direction of the soft bearing surface.

We compare the results of our simulations to those of other published works to check the validity and accuracy of our numerical model, including the lubricant film pressure and load-carrying capacity results of [33,40], and the cavitation results of [38,41].

2.2. Simulations and Analysis

Figure 2 shows a flow chart of a typical (soft) EHL simulation, which starts by specifying the separation between the bearing surfaces and then iterating between the lubricant film pressure solution (finite difference and Reynolds equation with HS, RE, or JFO cavitation model) and the bearing surface deformation solution (finite element and linear elastic equations), until they simultaneously converge. We add additional constraints to the (soft) EHL simulation by introducing an outer loop to the lubricant film pressure and bearing surface deformation calculation. For instance, in Figure 2, we included an additional loop to maintain a specific bearing load-carrying capacity, which requires an additional equation to converge simultaneously with the lubricant film pressure and deformation equations.

These multiple levels of convergence illustrate the complexity of (soft) EHL simulations and underscore the importance of understanding convergence at all levels of the simulations.

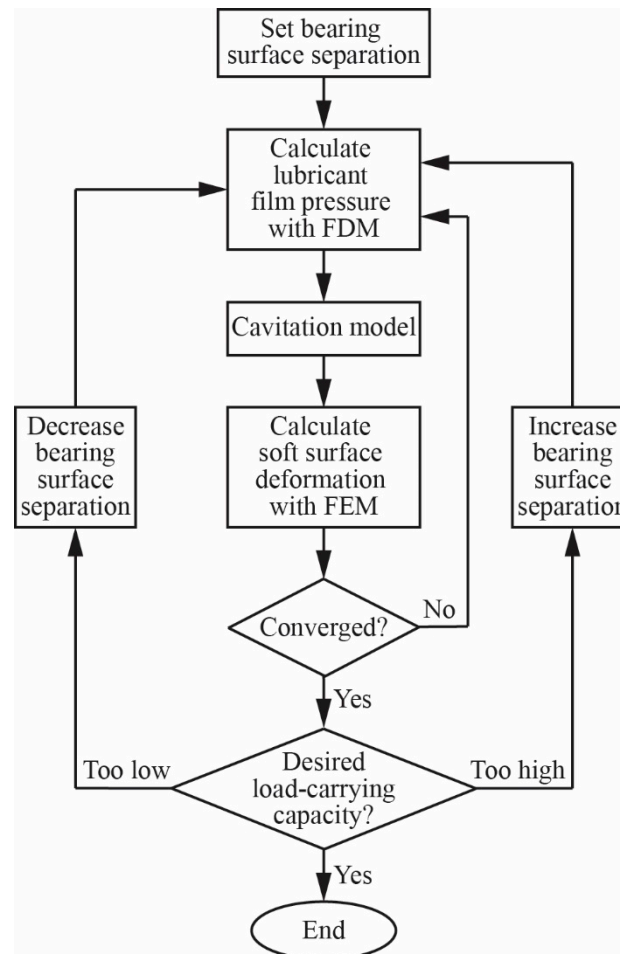


Figure 2. Flow-chart of a typical (soft) EHL simulation.

EHL simulations also require defining convergence criteria and metrics to determine what constitutes convergence of each of the equations that we solve simultaneously. Multiple methods exist to evaluate convergence; each method involves comparing the simulation result between two successive iterations. Different metrics of convergence include the average, maximum, or L2-norm of the difference between two successive iterations of the lubricant film pressure or bearing surface deformation solutions [7]. The simulation achieves convergence when the convergence metric becomes smaller than the pre-defined convergence criterion.

Furthermore, we must also ensure mesh convergence for both the finite difference discretization to calculate the lubricant film pressure, and for the finite element mesh to calculate the elastic deformation of the soft bearing surface. In both simulations, the discretization must be sufficiently fine to resolve the gradients of the lubricant film pressure or deformation solutions, respectively.

First, we study mesh convergence by varying the finite difference discretization (i.e., number of nodes per unit cell N) and convergence criterion α of the lubricant film pressure calculation within a single texture feature, while maintaining constant texture design and bearing operating parameters. Second, we evaluate convergence of the finite element mesh (i.e., number of finite elements N_e) for the deformation calculation. Finally, we determine the effect of the cavitation model and different convergence metrics on the convergence of the soft EHL simulations. To accomplish this, we perform EHL simulations in which

we solve Equations (2) and (3), considering different cavitation models of Table 1, and following the methodology of Figure 2. Table 2 summarizes the different parameters that we consider in this work, and their corresponding ranges.

Table 2. Parameters used in the convergence studies of the lubricant film pressure and deformation calculations.

Parameter	Minimum	Maximum	Nominal
Bearing separation, δ	-	-	0.045
Texture density, S_p	-	-	0.20
Aspect ratio, ε	0.01	0.09	0.05
Flow factor, λ	0.06	0.30	0.30
Number of nodes, N	101	601	301
Number of elements, N_e	4	36	20
Convergence criterion, α	10^{-5}	10^{-1}	10^{-3}

Throughout the convergence study, we quantify the local, average, and maximum values of the lubricant film pressure and the soft bearing surface deformation, as well as the lubricant film pressure and deformation gradients, and the number of successive iterations to achieve convergence, all as a function of the different convergence criteria and metrics.

3. Results and Discussion

3.1. Mesh Convergence

Figure 3a,b shows the non-dimensional average P_{avg} and maximum P_{max} lubricant film pressure and Figure 3c shows the number of iterations until convergence, as a function of the number of nodes per square unit cell N of the finite difference scheme, and for different values of the L2 norm convergence criterion (different marker types), using constant bearing operating parameters ($\lambda = 0.300$, $\delta = 0.045$) and texture design parameters ($\varepsilon = 0.05$, $S_p = 0.20$). Inset images illustrate the local non-dimensional lubricant film pressure (red) along the center line within a single texture feature (black). Additionally, Figure 4a,b shows the lubricant film pressure gradient in the x - and y -directions, respectively, also as a function of the number of nodes per square unit cell N of the finite difference scheme, and for different values of the L2 norm convergence criterion (different marker types), corresponding to the simulation results of Figure 3.

From Figure 3a,b, we observe that the lubricant film pressure depends on both the number of nodes per unit cell in the finite difference scheme N , and the L2 norm convergence criterion α . The non-dimensional average and maximum lubricant film pressure approach a constant value with an increasing number of nodes per unit cell, thus indicating convergence. Convergence occurs because accurately resolving the lubricant film pressure gradient within a texture feature requires a minimum number of nodes and, thus, decreasing the spacing between adjacent nodes enables the solution to conform to the physical lubricant film pressure gradient. Additionally, a sufficiently stringent convergence criterion is required to determine the convergence. For instance, Figure 3a shows that when using a convergence criterion, $\alpha = 10^{-1}$ or 10^{-2} , the simulation does not converge to the correct solution, independent of the number of successive iterations. However, we observe that when using a convergence criterion, $\alpha < 10^{-3}$, the simulation eventually approaches the correct solution when using a sufficient number of nodes per unit cell N . Figure 3c shows that the number of successive iterations to achieve a converged solution increases with the increasing number of nodes per unit cell, and with decreasing convergence criterion (more stringent), as expected, because the simulation requires more iterations to reduce the variation between successive iterations of the solution to a value that is smaller than an increasingly stringent convergence criterion. Based on the simulations for a textured slider bearing in this work, we determine that $N = 301$ nodes per unit cell and a convergence

criterion $\alpha = 10^{-3}$ with the L2 norm convergence metric result in a converged solution. Using more nodes per unit cell or a more stringent convergence criterion would increase the computation time, without materially altering the result. For instance, Figure 3a shows that the average non-dimensional lubricant film pressure $P_{avg} = 5.73$ after 35,826 iterations (Figure 3c). For comparison, increasing the number of nodes per unit cell to $N = 601$ nodes per unit cell and reducing the convergence criterion to $\alpha = 10^{-5}$ resulted in an average non-dimensional lubricant film pressure $P_{avg} = 5.88$ after 557,796 iterations. Hence, this example illustrates that correctly performing a convergence study prior to performing a (soft) EHL simulation can substantially reduce the computation time, with negligible effect on the outcome of the simulation. The lubricant film pressure gradient results support the information of the average and maximum non-dimensional lubricant film pressure, and lead to the same conclusions in terms of selecting the minimum number of nodes per unit cell and the value of the convergence criterion.

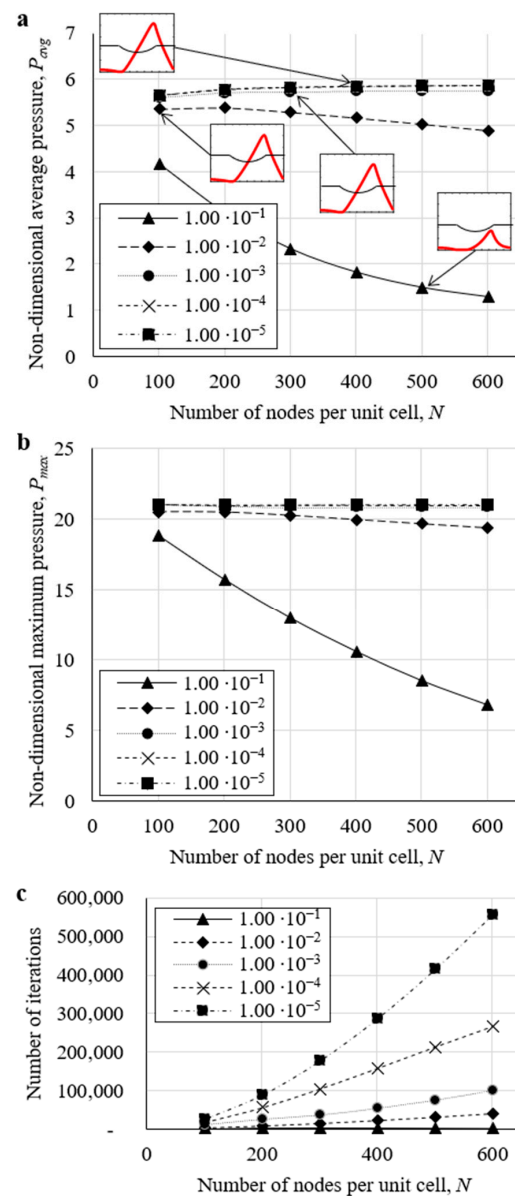


Figure 3. Mesh convergence of the lubricant film pressure calculation, showing non-dimensional (a) average pressure P_{avg} , (b) maximum pressure P_{max} , and (c) number of iterations until convergence, as a function of the number of nodes per unit cell of a texture feature N in the finite difference scheme, for different convergence criteria (different marker types) of the L2 norm convergence metric.

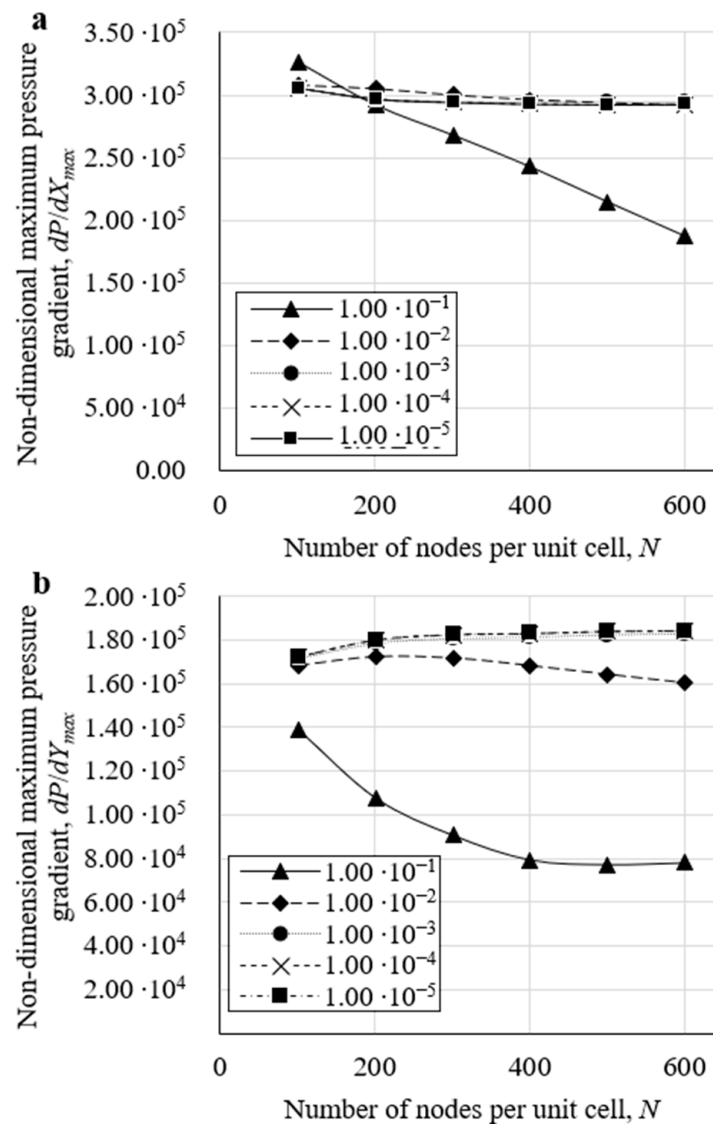


Figure 4. Mesh convergence of the lubricant film pressure gradient, showing non-dimensional (a) maximum pressure gradient dP/dX_{max} in the x -direction, and (b) dP/dY_{max} in the y -direction, as a function of the number of nodes per unit cell of a texture feature N in the finite difference scheme, for different convergence criteria (different marker types) of the L2 norm convergence metric.

Figure 5 shows the non-dimensional maximum deformation $D_{max} = \max(d(x,y))/2r_p$ as a function of the number of finite elements N_e along the length (x -direction) of the bearing, and for different number of elements in the thickness (z -direction) of the soft bearing material (different marker types), using a constant set of bearing operating parameters ($\lambda = 0.300$, $\delta = 0.045$) and texture design parameters ($\varepsilon = 0.05$, $S_p = 0.20$). Inset images illustrate the local non-dimensional bearing surface deformation (blue) along the center line opposite to a single texture feature (black). We obtained the deformation after applying the converged solution of the lubricant film pressure (using $N = 301$ nodes per unit cell with a convergence criterion $\alpha = 10^{-3}$ and using the L2 norm convergence metric) as a pressure load to the deformable bearing surface.

From Figure 5, we observe that increasing the number of elements along the length of the bearing N_e causes the maximum deformation D_{max} to converge to the correct physical solution. The finite element method approximates the deformation solution between nodes using a shape function and, thus, the accuracy of the solution increases when the shape function approximates the physical solution more closely, which usually occurs

with an increasing number of finite elements N_e , when the order of the polynomial shape function remains constant. Here, the deformation of the soft surface under the pressure load follows a higher-order (quadratic) polynomial and, therefore, increasing the number of elements and, consequently, number of nodes, increases the accuracy with which the shape function approximates the physical solution. We also observe that the number of elements in the thickness direction of the FE model has a minimal effect on the maximum surface deformation (the different marker types overlap), because the applied pressure load varies in the x - and y -directions yet remains constant in the z -direction. Based on the simulations for a textured slider bearing in this work, we select a converged solution for the FE model based on 20 elements along the length of the bearing (x -direction) and 40 elements in the thickness direction of the soft material (z -direction). Increasing the number of elements in the FE model to 36 along the length of the bearing and 40 elements in the thickness direction only changes the solution by less than 0.4%, but increases the time of convergence by 93.0%.

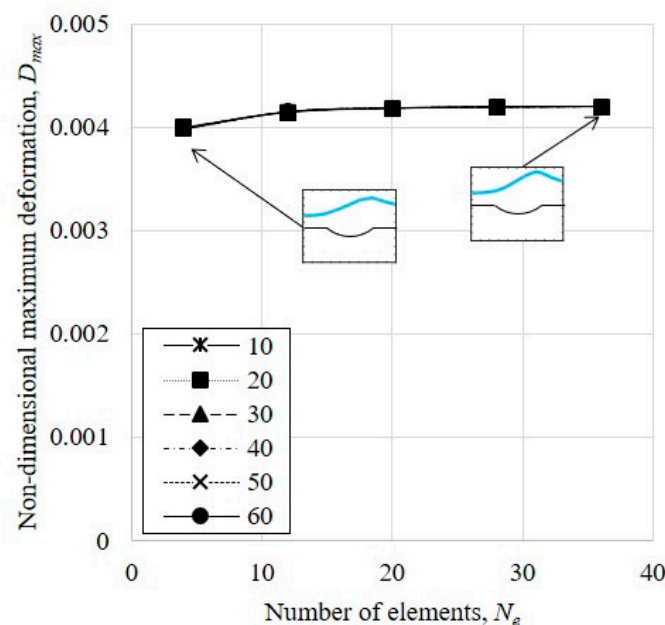


Figure 5. Mesh convergence of the deformation of the soft bearing surface, showing non-dimensional maximum deformation D_{max} as a function of the number of elements along the length of the bearing N_e , for different number of elements in the thickness direction of the soft material (different marker types).

3.2. Texture Geometry and Bearing Operating Conditions

Figure 6 shows the maximum P_{max} and average P_{avg} non-dimensional lubricant film pressure solution for the highest number of nodes per unit cell ($N = 601$) and the strictest convergence criterion ($\alpha = 10^{-5}$) as a function of (a) the texture aspect ratio ε (with $\lambda = 0.30$, $S_p = 0.20$) and (b) the non-dimensional flow factor λ (with $\varepsilon = 0.05$, $S_p = 0.20$). From Figure 6, we observe that the lubricant film pressure increases with an increasing texture aspect ratio ε because the displaced volume of lubricant increases (assuming a constant texture feature radius). The lubricant film pressure also increases with an increasing flow factor λ , because an increasing flow factor implies an increasing lubricant viscosity μ or relative sliding velocity U between the bearing surfaces. The incremental increase in lubricant film pressure decreases with the incremental increase in the texture aspect ratio because cavitation plays an increasingly important role with the increasing texture aspect ratio, and eventually prevents the lubricant film pressure from increasing further.

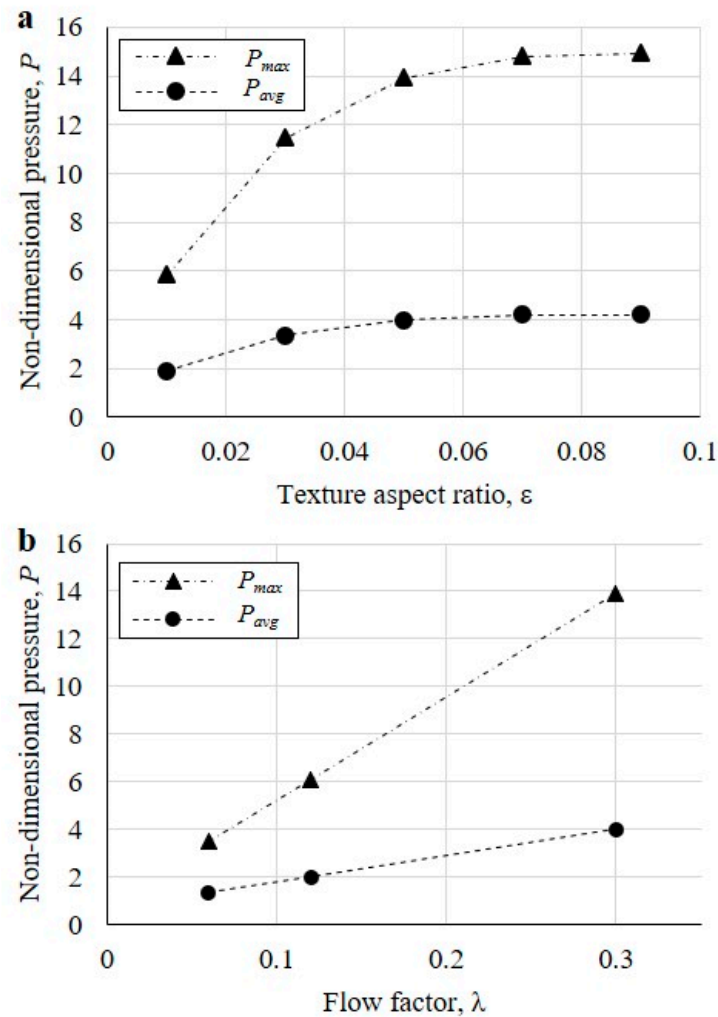


Figure 6. Maximum P_{max} and average P_{avg} non-dimensional lubricant film pressure solution for the strictest convergence criterion ($N = 601$, $\alpha = 10^{-5}$) as a function of (a) the texture aspect ratio ϵ (with $\lambda = 0.30$, $S_p = 0.20$) and (b) the non-dimensional flow factor λ (with $\epsilon = 0.05$, $S_p = 0.20$).

We derive best-fit equations for the maximum P_{max} and average P_{avg} non-dimensional lubricant film pressure as a function of the number of nodes per unit cell N , using the least-squares approach, for different values of the convergence criterion α , texture aspect ratio ϵ , and flow factor λ . These best-fit equations take the form of $P = aN^b$, where P is the (average or maximum) lubricant film pressure, N is the number of nodes per unit cell, a is a coefficient related to the magnitude of the lubricant film pressure, and b is an exponent that describes how quickly the lubricant film pressure changes with the number of nodes. These best-fit equations fit the simulation data well, resulting in an R^2 -value > 0.9 for almost all parameter combinations. Figure 7a shows the best-fit coefficient a , and Figure 7b shows the best-fit exponent b as a function of the texture aspect ratio ϵ . We observe that the best-fit coefficient a increases with an increasing texture aspect ratio ϵ because the lubricant film pressure increases with the texture aspect ratio. We also note that the best-fit exponent b decreases with an increasing texture aspect ratio ϵ because the lubricant film pressure is more sensitive to the number of nodes per unit cell with an increasing texture aspect ratio as a result of the increasing lubricant film pressure gradient.

We also determine the number of nodes per unit cell N and the convergence criterion α in combination with the L2 norm convergence metric, which leads to a converged lubricant pressure solution as a function of the texture aspect ratio ϵ and flow factor λ . Hence, we select the smallest number of nodes per unit cell N and convergence criterion α that cause

the result to be less than 2% different to the results obtained with the strictest convergence criterion, shown in Figure 6 (i.e., $N = 601$, $\alpha = 10^{-5}$). Figure 8 shows the number of nodes per unit cell N of the lubricant film pressure solution as a function of (a) the texture aspect ratio ε and (b) as a function of the flow factor λ .

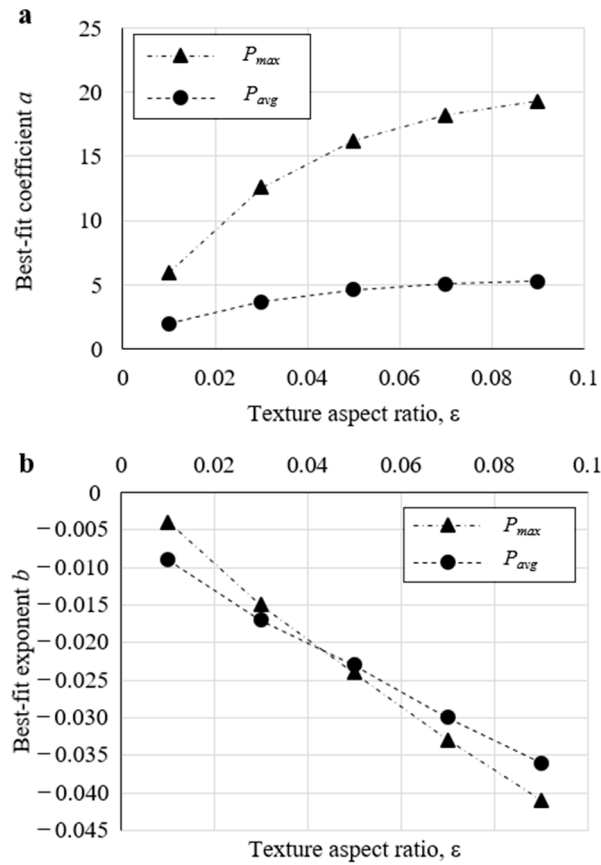


Figure 7. (a) Best-fit coefficient a and (b) best-fit exponent b as a function of the texture aspect ratio ε , for both the maximum P_{max} and average P_{avg} lubricant film pressure.

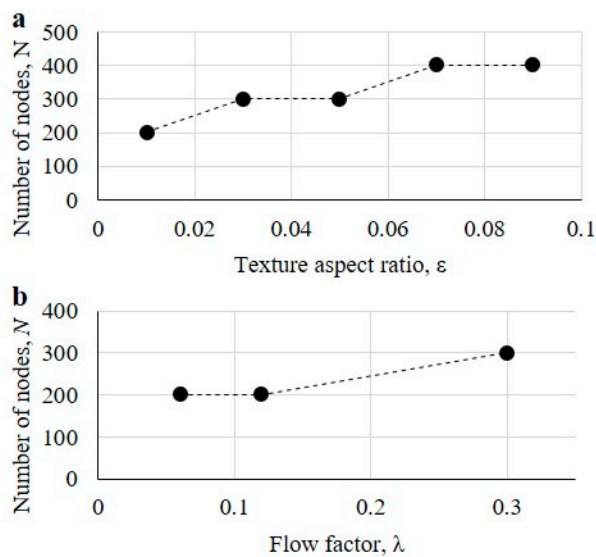


Figure 8. Number of nodes per unit cell N of the lubricant film pressure solution as a function of (a) the texture aspect ratio ε and (b) the flow factor λ .

From Figure 8, we observe that the number of nodes per unit cell N required to achieve a converged lubricant film pressure solution increases with an increasing texture aspect ratio ε and increasing flow factor λ , because the lubricant film pressure gradient increases with an increasing texture aspect ratio and flow factor, requiring an increasing number of nodes per unit cell N to accurately resolve the increasing pressure gradients. The convergence criterion α required to achieve a converged lubricant film pressure solution remains $\alpha = 10^{-3}$ independent of the texture aspect ratio, but decreases to $\alpha = 10^{-4}$ for $\lambda = 0.12$ and $\lambda = 0.06$.

These results have implications for parameter studies of different texture design parameters and EHL bearing operating conditions. The error of numerical simulations with a constant number of nodes per unit cell N and convergence criterion α changes as a function of the texture geometry and bearing operating conditions. This variable error must be balanced with the computational cost, which increases with increasing number of nodes and more strict convergence criterion (see Figure 3c). We determine the parabolic best-fit curves of the form $I = aN^2 + bN + c$, where I is the number of successive iterations, N is the number of nodes per unit cell, and a , b , and c are regression coefficients, to mathematically describe the increasing computational cost with an increasing number of nodes per unit cell N . Table 3 shows the regression coefficients for the best-fit equations and the corresponding R^2 values to quantify goodness of fit as a function of the convergence criterion α . We observe that for large values of the convergence criterion α , a is close to zero, indicating an almost linear increase in computation time with the number of nodes per unit cell N . However, we observe that a approaches one with increasingly strict convergence criterion α , indicating a more than proportional increase in the number of iterations I with the increasing number of nodes per unit cell N . For the range of texture aspect ratio ε and flow factor λ considered in this work, selecting $N = 301$ and $\alpha = 10^{-3}$ resulted in a maximum error of approximately 2.5% for the average non-dimensional lubricant film pressure (compared to the result obtained with $N = 601$ and $\alpha = 10^{-5}$), for a texture aspect ratio of 0.09 with $\lambda = 0.30$.

Table 3. Coefficients for the best-fit curves for the number of iterations as a function of the number of nodes, of the form $I = aN^2 + bN + c$ (see Figure 3c).

Convergence Criterion	a	b	c	R^2
10^{-1}	-0.017	12.636	913.5	0.860
10^{-2}	0.050	37.120	-549.5	1.000
10^{-3}	0.170	54.476	4667.4	0.998
10^{-4}	0.182	373.550	-23,084.0	0.999
10^{-5}	0.988	377.260	-23,885.0	1.000

3.3. Convergence Metric and Cavitation Model

We evaluate the effect of the convergence metric on the convergence of the lubricant film pressure simulations by comparing the L2 norm, average, and maximum convergence metrics. Figure 9a–c shows the non-dimensional maximum P_{max} and average P_{avg} lubricant film pressure, the number of nodes per unit cell N , and the convergence criterion α required to achieve a converged lubricant film pressure solution, respectively, versus the convergence metrics, and a typical example simulation with $\varepsilon = 0.050$, $S_p = 0.200$, $\delta = 0.045$, and $\lambda = 0.300$.

From Figure 9, we observe that all convergence metrics result in the same (maximum P_{max} and average P_{avg}) non-dimensional lubricant film pressure. However, the number of nodes per unit cell N and convergence criterion α required to achieve convergence are different. The L2 norm is the strictest convergence metric and requires the smallest number of nodes per unit cell and largest convergence criterion. In contrast, the average is the least strict convergence metric, which requires the highest number of nodes and the smallest convergence criterion to achieve convergence. When using the average as the convergence

metric, a large number of nodes can satisfy the convergence criterion after only one iteration. With 601 nodes, none of the convergence criteria are sufficiently stringent to force more than one iteration of Equation (2). With 501 nodes, only the strictest convergence criterion ($\alpha = 10^{-5}$) completes more than a single iteration. The average convergence metric is more likely to indicate convergence with an increasing number of nodes per unit cell because a large difference between the lubricant film pressure solution of two successive iterations at one node is averaged over all nodes. In contrast, the maximum and L2 norm convergence metrics do not allow a large difference between the lubricant film pressure solution of two successive iterations at one node to be averaged over all nodes and become increasingly strict with an increasing number of nodes per unit cell.

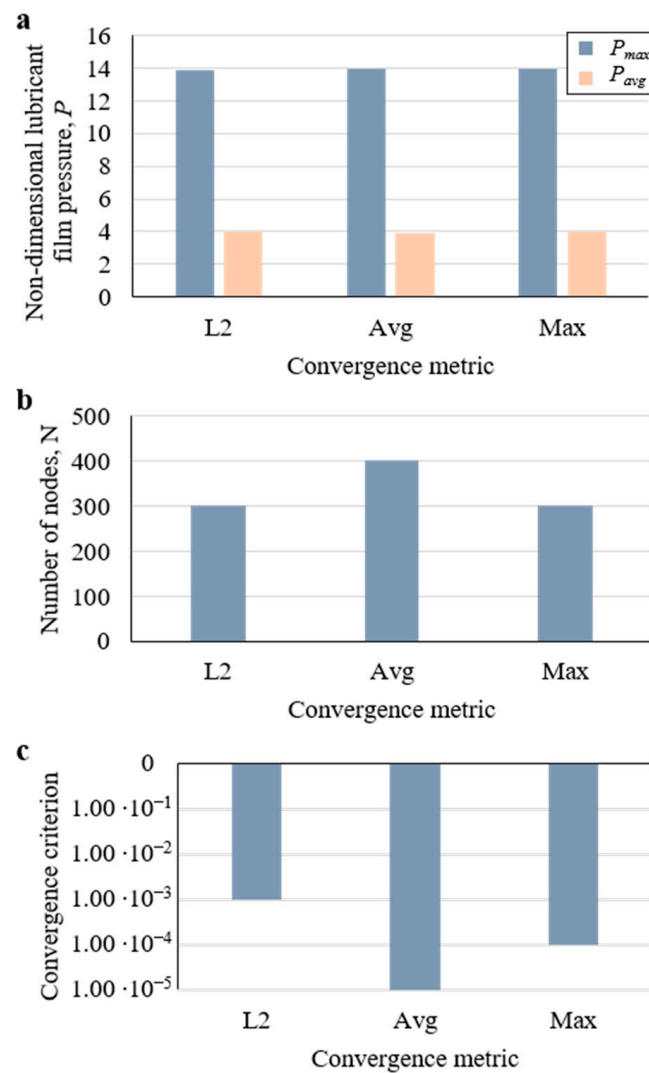


Figure 9. (a) Maximum P_{max} and average P_{avg} non-dimensional lubricant film pressure, (b) number of nodes per unit cell N , and (c) convergence criterion α required to achieve a converge lubricant film pressure solution, versus the convergence metrics, and a typical example simulation with $\varepsilon = 0.050$, $S_p = 0.200$, $\delta = 0.045$, and $\lambda = 0.300$.

We also consider the effect of the cavitation model on the convergence of the lubricant film pressure solution by simulating the RE, HS, and JFO cavitation models for a typical example with $\varepsilon = 0.050$, $S_p = 0.200$, $\delta = 0.045$, and $\lambda = 0.300$. Figure 10a shows the maximum P_{max} and average P_{avg} non-dimensional lubricant film pressure and Figure 10b shows the maximum non-dimensional lubricant film pressure gradient dP/dX_{max} and dP/dY_{max} as a function of the cavitation model (HS, RE, and JFO, see Section 2).

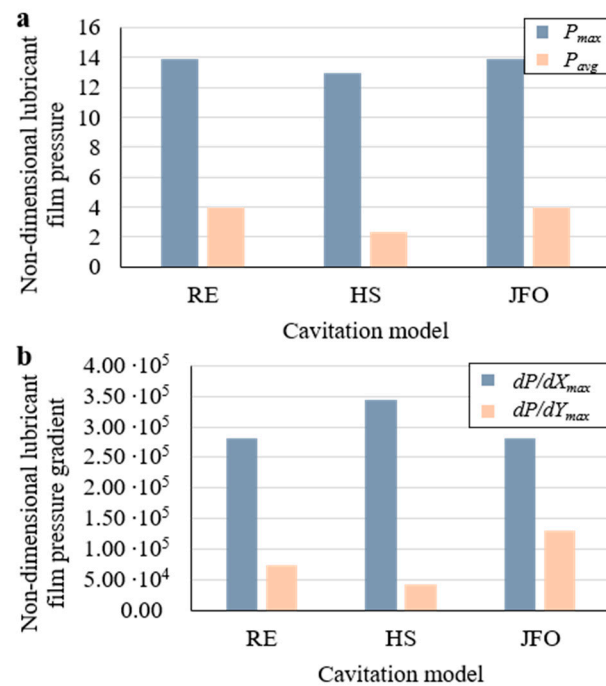


Figure 10. (a) Non-dimensional maximum P_{max} and average P_{avg} lubricant film pressure and (b) maximum lubricant film pressure gradient dP/dX_{max} and dP/dY_{max} in x - and y -directions as a function of the cavitation model.

From Figure 10, we observe that the RE and JFO cavitation models find almost identical results for both the non-dimensional lubricant film pressure and the lubricant film pressure gradient in the x -direction. The JFO cavitation model simulates a higher lubricant film pressure gradient in the y -direction because it predicts a larger cavitation region than the RE cavitation model. The HS cavitation model underestimates the lubricant film pressure compared to the other cavitation models, which is as expected. To achieve convergence within 2% of the strictest converged lubricant film pressure result, we observe a different number of nodes, number of successive iterations, and convergence criterion for each cavitation model (see Table 4). We observe that the HS cavitation model requires more nodes, a stricter convergence criterion, and many more iterations to achieve convergence compared to the other cavitation models. As implemented here, the HS cavitation model is the slowest cavitation model to reach convergence and it is also known to be the least accurate because it does not conserve mass and it results in a non-differentiable lubricant film pressure. The JFO cavitation model requires fewer nodes, yet more successive iterations for convergence than the RE cavitation model, because it requires convergence of both the lubricant film pressure and the film content parameter (see Equation (3)).

Table 4. Convergence of different cavitation models.

Cavitation Model	Number of Nodes per Unit Cell, N	Convergence Criterion	Number of Successive Iterations
RE	301	10^{-3}	28,473
HS	401	10^{-4}	240,686
JFO	201	10^{-3}	39,292

3.4. Additional Considerations for Soft EHL Convergence

Soft EHL simulations require additional consideration compared to EHL simulations to obtain convergence because of the sensitivity of the deformation of the soft bearing surface to the changes in the lubricant film pressure. When considering the convergence of (soft)

EHL simulations in textured slider bearings, researchers must consider the convergence metric and criterion and the number of nodes at each level of their simulations. These convergence parameters must be chosen carefully in consideration of other simulation parameters, such as texture design and bearing operating parameters, bearing surface material properties, and the cavitation model. Convergence studies must evaluate a range of convergence parameters and metrics to ensure that they are sufficiently stringent to resolve the gradients in the numerical solution of the lubricant film pressure and bearing material deformation. In our previous work (see [13]), we compared the lubricant film pressure in textured slider bearings with different cavitation models and showed that the JFO cavitation model is more prone to instability and generally requires more iterations between converged lubricant film pressure and bearing surface deformation results than the RE model. These convergence concerns with JFO cavitation models have been well-documented (see, e.g., [41]), though recently, more efficient implementations of the JFO boundary conditions have been proposed by Woloszynski et al. [42] and Biboulet and Lubrecht [43].

4. Conclusions

We conclude the following:

- Performing a comprehensive convergence study of both the lubricant film pressure and the bearing surface deformation calculations is crucial to achieving accurate and converged solutions of (soft) EHL simulations. A convergence study assists with the selection of the discretization/mesh size and convergence criterion for a chosen convergence metric to minimize the computational cost of the simulations. The accuracy of (soft) EHL simulations of textured bearing surfaces increases with an increasing number of nodes and decreasing convergence criterion because a small spacing between nodes and a sufficient number of successive iterations are required to accurately resolve the gradients and reduce the error in both finite difference and finite element simulations of the lubricant film pressure and the bearing surface deformation, respectively. Additionally, the computational cost of the simulations increases with an increasing number of nodes and decreasing convergence criterion because more successive iterations are required to achieve convergence.
- Specific to (soft) EHL simulations of textured bearing surfaces, we determine that the number of nodes per unit cell, required to achieve convergence of the lubricant film pressure, increases with an increasing texture aspect ratio and increasing flow factor. This is because the lubricant film pressure increases with an increasing texture aspect ratio and increasing flow factor, which requires a finer grid and, thus, more nodes per unit cell to accurately resolve the pressure gradients.
- The choice of cavitation algorithm affects the convergence of the lubricant film pressure simulations. Specifically, the half-Sommerfeld cavitation algorithm requires the most nodes per unit cell and smallest convergence criterion, increasing the number of successive iterations by an order of magnitude compared to the Reynolds and JFO cavitation algorithms. The JFO cavitation algorithm requires fewer nodes per unit cell, yet it still requires more successive iterations for convergence than the Reynolds cavitation algorithm because of the additional complexity of simultaneously solving the lubricant film pressure and the fractional film content.

Author Contributions: Conceptualization, B.R.; Methodology, Q.A.; Software, Q.A.; Validation, Q.A. and B.R.; Formal analysis, Q.A. and B.R.; Investigation, Q.A. and B.R.; Resources, B.R.; Data curation, Q.A.; Writing—original draft, Q.A. and B.R.; Writing—review & editing, Q.A. and B.R.; Visualization, B.R.; Funding acquisition, B.R. All authors have read and agreed to the published version of the manuscript.

Funding: This research was funded by the National Institutes of Health and the National Institute of Arthritis and Musculoskeletal and Skin Diseases grant number 1R03AR066826-01A1 and the APC was funded by Brigham Young University and Virginia Polytechnic Institute and State University.

Data Availability Statement: The data presented in this study are available on request from the corresponding author.

Conflicts of Interest: The authors declare no conflict of interest.

References

1. Rahmani, R.; Rahnejat, H.; Fitzsimons, B.; Dowson, D. The effect of cylinder liner operating temperature on frictional loss and engine emissions in piston ring conjunction. *Appl. Energy* **2017**, *191*, 568–581. [\[CrossRef\]](#)
2. Kotzalas, M.N.; Doll, G.L. Tribological advancements for reliable wind turbine performance. *Philos. Trans. R. Soc. Lond. A Math. Phys. Sci.* **2010**, *368*, 4829–4850. [\[CrossRef\]](#) [\[PubMed\]](#)
3. Chakravarty, R.; Elmallah, R.D.K.; Cherian, J.J.; Kurtz, S.M.; Mont, M.A. Polyethylene wear in knee arthroplasty. *J. Knee Surg.* **2015**, *28*, 370–375. [\[CrossRef\]](#)
4. Borjali, A.; Monson, K.; Raeymaekers, B. Predicting the polyethylene wear rate in pin-on-disc experiments in the context of prosthetic hip implants: Deriving a data-driven model using machine learning methods. *Tribol. Int.* **2019**, *133*, 101–110. [\[CrossRef\]](#) [\[PubMed\]](#)
5. Hamrock, B.J.; Schmid, B.J.; Jacobson, B.O. *Fundamentals of Fluid Film Lubrication*; CRC Press: Boca Raton, FL, USA, 2004.
6. Mate, C.M.; Carpick, R.W. *Tribology on the Small Scale: A Modern Textbook on Friction, Lubrication, and Wear*; Oxford University Press: Oxford, UK, 2019.
7. Dowson, D. Elastohydrodynamic and micro-elastohydrodynamic lubrication. *Wear* **1995**, *190*, 125–138. [\[CrossRef\]](#)
8. Allen, Q.; Raeymaekers, B. Surface texturing of prosthetic hip implant bearing surfaces: A review. *J. Tribol.* **2021**, *143*, 040801. [\[CrossRef\]](#) [\[PubMed\]](#)
9. Sadowski, P.; Stupkiewicz, S. Friction in lubricated soft-on-hard, hard-on-soft and soft-on-soft sliding contacts. *Tribol. Int.* **2019**, *129*, 246–256. [\[CrossRef\]](#)
10. Zhang, H.; Hua, M.; Dong, G.N.; Zhang, D.Y.; Chin, K.S. A mixed lubrication model for studying tribological behaviors of surface texturing. *Tribol. Int.* **2016**, *93*, 583–592. [\[CrossRef\]](#)
11. Allen, Q.; Raeymaekers, B. Maximizing the lubricant film thickness between a rigid microtextured and a smooth deformable surface in relative motion, using a soft elasto-hydrodynamic lubrication model. *J. Tribol.* **2020**, *142*, 071802. [\[CrossRef\]](#)
12. Allen, Q.; Raeymaekers, B. The effect of texture floor profile on the lubricant film thickness in a textured hard-on-soft bearing with relevance to prosthetic hip implants. *J. Tribol.* **2021**, *143*, 021801. [\[CrossRef\]](#)
13. Allen, Q.; Raeymaekers, B. Soft EHL simulations of lubricant film thickness in textured hard-on-soft bearings considering different cavitation models, in the context of prosthetic hip implants. *Tribol. Lett.* **2021**, *69*, 118. [\[CrossRef\]](#)
14. Ma, C.; Sun, J.; Wang, Y.; Yu, B.; Yu, Q.; Tu, Q. On the optimum dimple depth-over-diameter ratio for textured surfaces. *Adv. Mech. Eng.* **2017**, *9*, 1687814017720085. [\[CrossRef\]](#)
15. Gong, J.; Jin, Y.; Liu, Z.; Jiang, H.; Xiao, M. Study on influencing factors of lubrication performance of water-lubricated micro-groove bearing. *Tribol. Int.* **2019**, *129*, 390–397. [\[CrossRef\]](#)
16. Shinkarenko, A.; Kligerman, Y.; Etsion, I. The effect of elastomer surface texturing in soft elasto-hydrodynamic lubrication. *Tribol. Lett.* **2009**, *36*, 95–103. [\[CrossRef\]](#)
17. Qiu, Y.; Khonsari, M.M. On the prediction of cavitation in dimples using a mass-conservative algorithm. *J. Tribol.* **2009**, *131*, 041702. [\[CrossRef\]](#)
18. Ausas, R.; Ragot, P.; Leiva, J.; Jai, M.; Bayada, G.; Buscaglia, G.C. The impact of the cavitation model in the analysis of microtextured lubricated journal bearings. *J. Tribol.* **2007**, *129*, 868–875. [\[CrossRef\]](#)
19. de Vicente, J.; Stokes, J.R.; Spikes, H.A. The frictional properties of Newtonian fluids in rolling—Sliding soft-EHL contact. *Tribol. Lett.* **2005**, *20*, 273–286. [\[CrossRef\]](#)
20. Su, B.; Huang, L.; Huang, W.; Wang, X. The load carrying capacity of textured sliding bearings with elastic deformation. *Tribol. Int.* **2017**, *109*, 86–96. [\[CrossRef\]](#)
21. Hooke, C.J.; O'Donoghue, J.P. Elastohydrodynamic lubrication of soft highly deformed contacts. *J. Mech. Eng. Sci.* **1972**, *14*, 34–48. [\[CrossRef\]](#)
22. Jones, M.B.; Fulford, G.R.; Please, C.P.; McElwain, D.L.S.; Collins, M.J. Elastohydrodynamics of the eyelid wiper. *Bull. Math. Biol.* **2008**, *70*, 323–343. [\[CrossRef\]](#)
23. Arnold, D.N. Stability, consistency, and convergence of numerical discretizations. In *Encyclopedia of Applied and Computational Mathematics*; Springer: Berlin/Heidelberg, Germany, 2015; pp. 1358–1364. [\[CrossRef\]](#)
24. Qiu, M.; Raeymaekers, B. The load-carrying capacity and friction coefficient of incompressible textured parallel slider bearings with surface roughness inside the texture features. *Proc. Inst. Mech. Eng. Part J J. Eng. Tribol.* **2015**, *229*, 547–556. [\[CrossRef\]](#)
25. Qiu, M.; Minson, B.R.; Raeymaekers, B. The effect of texture shape on the friction coefficient and stiffness of gas-lubricated parallel slider bearings. *Tribol. Int.* **2013**, *67*, 278–288. [\[CrossRef\]](#)
26. Venner, C.H.; Lubrecht, A.A. *Multilevel Methods in Lubrication*; Dowson, D., Ed.; Elsevier: New York, NY, USA, 2000; ISBN 0 444 5053 2.
27. Qiu, M.; Delic, A.; Raeymaekers, B. The effect of texture shape on the load-carrying capacity of gas-lubricated parallel slider bearings. *Tribol. Lett.* **2012**, *48*, 315–327. [\[CrossRef\]](#)

28. Manser, B.; Belaidi, I.; Hamrani, A.; Khelladi, S.; Bakir, F. Texture shape effects on hydrodynamic journal bearing performances using mass-conserving numerical approach. *Tribol. Mater. Surf. Interfaces* **2020**, *14*, 33–50. [[CrossRef](#)]
29. Zhang, H.; Hua, M.; Dong, G.Z.; Zhang, D.Y.; Chen, W.J.; Dong, G.N. Optimization of texture shape based on Genetic Algorithm under unidirectional sliding. *Tribol. Int.* **2017**, *115*, 222–232. [[CrossRef](#)]
30. Shen, C.; Khonsari, M.M. Numerical optimization of texture shape for parallel surfaces under unidirectional and bidirectional sliding. *Tribol. Int.* **2015**, *82*, 1–11. [[CrossRef](#)]
31. Etsion, I. State of the Art in Laser Surface Texturing. *J. Tribol.* **2005**, *127*, 248–253. [[CrossRef](#)]
32. Cunha, A.; Elie, A.-M.; Plawinski, L.; Serro, A.P.; Botelho Do Rego, A.M.; Almeida, A.; Urdaci, M.C.; Durrieu, M.-C.; Vilar, R. Femtosecond laser surface texturing of titanium as a method to reduce the adhesion of *Staphylococcus aureus* and biofilm formation. *Appl. Surf. Sci.* **2016**, *360*, 485–493. [[CrossRef](#)]
33. Chyr, A.; Qiu, M.; Speltz, J.W.; Jacobsen, R.L.; Sanders, A.P.; Raeymaekers, B. A patterned microtexture to reduce friction and increase longevity of prosthetic hip joints. *Wear* **2014**, *315*, 51–57. [[CrossRef](#)]
34. Borjali, A.; Langhorn, J.; Monson, K.; Raeymaekers, B. Using a patterned microtexture to reduce polyethylene wear in metal-on-polyethylene prosthetic bearing couples. *Wear* **2017**, *392*, 77–83. [[CrossRef](#)]
35. Langhorn, J.; Borjali, A.; Hippensteel, E.; Nelson, W.; Raeymaekers, B. Microtextured CoCrMo alloy for use in metal-on-polyethylene prosthetic joint bearings: Multi-directional wear and corrosion measurements. *Tribol. Int.* **2018**, *124*, 178–183. [[CrossRef](#)]
36. Hori, Y. *Hydrodynamic Lubrication*; Springer-Verlag: Tokyo, Japan, 2006.
37. Liu, H.; Xu, H.; Ellison, P.J.; Jin, Z. Application of computational fluid dynamics and fluid-structure interaction method to the lubrication study of a rotor-bearing system. *Tribol. Lett.* **2010**, *38*, 325–336. [[CrossRef](#)]
38. Wang, L.; Wang, W.; Wang, H.; Ma, T.; Hu, Y. Numerical analysis on the factors affecting the hydrodynamic performance for the parallel surfaces with microtextures. *J. Tribol.* **2014**, *136*, 021702. [[CrossRef](#)]
39. Elrod, H.G. A cavitation algorithm. *J. Lubr. Technol.* **1981**, *103*, 350–354. [[CrossRef](#)]
40. Shinkarenko, A.; Kligerman, Y.; Etsion, I. The effect of surface texturing in soft elasto-hydrodynamic lubrication. *Tribol. Int.* **2009**, *42*, 284–292. [[CrossRef](#)]
41. Fesanghary, M.; Khonsari, M.M. A modification of the switch function in the Elrod cavitation algorithm. *J. Tribol.* **2011**, *133*, 024501. [[CrossRef](#)]
42. Woloszynski, T.; Podsiadlo, P.; Stachowiak, G.W. Efficient solution to the cavitation problem in hydrodynamic lubrication. *Tribol. Lett.* **2015**, *58*, 18. [[CrossRef](#)]
43. Biboulet, N.; Lubrecht, A.A. Efficient solver implementation for reynolds equation with mass-conserving cavitation. *Tribol. Int.* **2018**, *118*, 295–300. [[CrossRef](#)]

Disclaimer/Publisher’s Note: The statements, opinions and data contained in all publications are solely those of the individual author(s) and contributor(s) and not of MDPI and/or the editor(s). MDPI and/or the editor(s) disclaim responsibility for any injury to people or property resulting from any ideas, methods, instructions or products referred to in the content.